Measurement of Broadband Temperature-Dependent Ultrasonic Attenuation and Dispersion Using Photoacoustics

Bradley E. Treeby, Benjamin T. Cox, Edward Z. Zhang, Sarah K. Patch, and Paul C. Beard

***Abstract*—The broadband ultrasonic characterization of biological fluids and tissues is important for the continued development and application of high-resolution ultrasound imaging modalities. Here, a photoacoustic technique for the transmission measurement of temperature-dependent ultrasonic attenuation and dispersion is described. The system uses a photoacoustic plane wave source constructed from a polymethylmethacrylate substrate with a thin optically absorbent layer. Broadband ultrasonic waves are generated by illuminating the absorbent layer with nanosecond pulses of laser light. The transmitted ultrasound waves are detected by a planar 7-μm high-finesse Fabry-Perot interferometer. Temperature-induced thickness changes in the Fabry-Perot interferometer are tracked to monitor the sample temperature and maintain the sensor sensitivity. The measured −6-dB bandwidth for the combined source and sensor is 1 to 35 MHz, with an attenuation corrected signal level at 100 MHz of −10 dB. The system is demonstrated through temperature-dependent ultrasound measurements in castor oil and olive oil. Power law attenuation parameters are extracted by fitting the experimental attenuation data to a frequency power law while simultaneously fitting the dispersion data to the corresponding Kramers-Krönig relation. The extracted parameters are compared with other calibration measurements previously reported in the literature.**

I. Introduction

The development of ultrasound as a diagnostic imaging modality has been coupled with extensive research into the ultrasonic properties of human tissue [1], [2]. These measurements typically cover the 1- to 10-MHz range, the range of most clinical diagnostic ultrasound systems. At these frequencies, the ultrasonic attenuation in tissue is comparatively low, facilitating the conventional *in vivo* imaging of deep anatomical structures [3]. Knowledge of the ultrasonic attenuation allows for pragmatic adjustments of the time-gain compensation, the most common approach for attenuation correction [4]. Similarly, knowledge of the ultrasonic impedance and sound speed allows for tissue identification and for depth and other topological information to be estimated. As transducer and signal processing technology has developed, imaging applications requiring increased resolution of superficial structures have progressively shifted to using higher frequencies [5]. For example, high-frequency ultrasonic imaging (HFUI), also called ultrasound biomicroscopy, has found many applications in the 40- to 60-MHz range [6], including within dermatology [7], oncology [8], and ophthalmology [9]. In addition to high-frequency pulse-echo type ultrasound, other emerging imaging modalities also use ultrasonic frequencies beyond the traditional diagnostic bandwidth. Of particular interest is photoacoustic tomography (PAT), which uses ultrasonic waves in the 1- to 40-MHz range generated by the photoacoustic effect [10].

The development of these ultrasound technologies brings with it a necessary re-characterization of the tissues and anatomical structures under investigation. For HFUI, it is entirely appropriate to use the same transducer technologies to conduct ultrasound transmission measurements *in vitro*. Such an approach has been used for the high-frequency ultrasonic characterization of several biological materials, including skin [11], ocular tissue [12], and vasculature and blood [13]. However, ultrasound transducers manufactured from lead zirconate titanate (PZT) and polyvinylidene difluoride (PVDF) typically exhibit a Gaussian-type frequency response about their center frequency [14]. Consequently, a transducer designed for HFUI will be inadequate for the simultaneous ultrasonic characterization of materials in the conventional diagnostic spectrum. This is also true for measurements made using scanning acoustic microscopy, an ultra-high frequency technique, which has also been applied to tissue characterization [15]. The actual requirement for the measurement bandwidth depends on the context of the intended application. In PAT, the localized absorption of light generates relatively broadband ultrasonic waves via thermoelastic expansion. Consequently, there is a requirement for the characterization of tissue structures and phantom materials over a broad frequency range (covering both the high-frequency and traditional diagnostic spectrums). Although the inclusion of attenuation data in PAT image reconstruction has only recently been considered [16], [17], the accurate modeling of photoacoustic wave propagation in tissue is an integral part of quantitative data extraction [18], [19]. The use of biological tissue and fluid samples at both body and room temperature is also common (e.g., human blood [20] and intercostal tissue [21]). The ultrasonic characterization of tissue and phantom materials at a variety of temperatures over a broadband frequency range is thus important for the continued development of the technology.

Manuscript received December 2, 2008; accepted April 19, 2009. This work was supported by the Engineering and Physical Sciences Research Council, UK.

B. E. Treeby, B. T. Cox, E. Z. Zhang, and P. C. Beard are with the Department of Medical Physics and Bioengineering, University College London, London, UK (e-mail: btreeby@mpb.ucl.ac.uk).

S. K. Patch is with the Department of Physics, University of Wisconsin-Milwaukee, Milwaukee, WI.

Digital Object Identifier 10.1109/TUFFC.2009.1231

0885–3010/$25.00 © 2009 IEEE

Here, a photoacoustic technique for the transmission measurement of ultrasonic attenuation and dispersion is described. The ultrasonic source is produced by illuminating a black paint layer on a polymethylmethacrylate (PMMA) substrate with short pulses of laser light. The generated plane waves propagate through a thin layer of attenuating test fluid and are detected by an optical ultrasound sensor. The sensor is constructed from a planar Fabry-Perot polymer film interferometer that is interrogated by a second laser. Changes in the optical thickness of the Fabry-Perot sensor are used to recover both pressure and temperature. A small area of measurement points are scanned and averaged to improve the fidelity of signal acquisition. The test signals are then processed relative to a reference measurement in distilled water to recover the attenuation parameters. The system is used to measure the temperature-dependent attenuation and dispersion of 2 reference materials: castor oil and olive oil. The changes in sound speed and power law attenuation parameters with temperature are described.

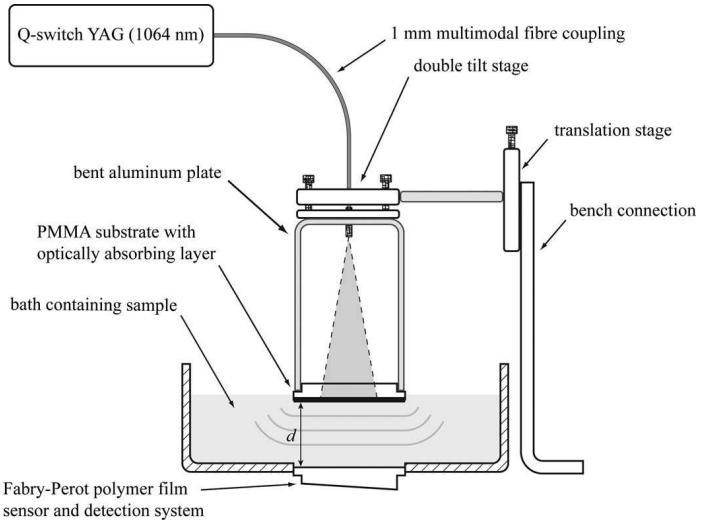

Fig. 1. Schematic of the experimental setup for the optical measurement of ultrasonic attenuation and dispersion.

II. Measurement System and Setup

A. Photoacoustic Ultrasonic Source

The generation of ultrasound via the thermoelastic expansion of thin optically absorbing layers has previously been discussed in relation to ultrasonic measurements in both solids and liquids [22]–[24]. The theoretical basis for the generation of these thermoelastic waves (one of several possible mechanisms for generating photoacoustic signals) has also been studied in detail [25], [26]. To maximize the efficiency of the conversion between the absorbed optical energy and the generated acoustic pressure, the optical energy must be deposited before the mass density of the absorbing layer has had time to change (a condition known as stress confinement). This condition is satisfied when the heating pulse occurs on a time scale much shorter than that for the sound to travel across the layer [27]. For thin absorbing layers (on the order of 100 μm), broadband ultrasonic waves can be efficiently generated via illumination with nanosecond laser pulses of high peak power. Under the conditions of stress confinement, the strength of the generated ultrasound wave is directly proportional to the amount of optical energy incident on the absorber. The proportionality constant is given by the nondimensional Grüneisen parameter, which has typical values on the order of 0.1.

Here, an ultrasonic plane wave source was created by illuminating a rectangular optical absorber with nanosecond laser pulses from a fiber-coupled laser. The laser source used was a Q-switched Nd:YAG (Ultra, Big Sky Laser Technologies, Bozeman, MT) operating at 1064 nm. The pulse duration, energy, and repetition frequency were 5.6 ns, 45 mJ, and 20 Hz, respectively. The absorber itself was constructed from a PMMA substrate ($10 \times 30 \times 50$ mm) with a thin layer of gloss black spray paint applied to the underside (on the order of 50 μm). The absorber and the laser fiber tip were aligned by a rigid connection made from thin aluminum plate with a separation distance of 135 mm (see Fig. 1). The beam divergence from the fiber tip was approximately 12°, giving an illumination spot radius of ∼14 mm. The strength of the source measured in distilled water using a needle hydrophone at a distance of 10 mm was 120 kPa.

B. Fabry-Perot Ultrasound Sensor

The optical detection of ultrasound has been studied in some detail, particularly in relation to PAT [28]–[31]. The most common approach is to use an etalon with 2 partially reflecting parallel mirrors separated by a small rigid spacer (i.e., a Fabry-Perot interferometer). The etalon is then interrogated by a focused laser beam. When an acoustic pressure is applied to the surface, the optical thickness of the etalon is modified, changing the interference pattern between the reflected light beams. By monitoring the intensity of the reflected signal using a photodiode, the acoustic pressure can thus be measured. The sensitivity of this detection can be maximized by selecting an interrogation wavelength close to where resonant interference occurs. For a high-finesse Fabry-Perot interferometer, this corresponds to a large drop (and thus a steep gradient) in the reflected optical power; see Fig. 2(a). Small changes in the optical thickness (and therefore acoustic pressure) can then be resolved [29]. For large sensors, the optimum wavelength selection can be completed separately for each interrogation position [29], [31]. This allows the sensitivity and linearity of the sensor to be maintained, regardless of any spatial variation in the unperturbed optical thickness. The relationship between the reflected optical power and the interrogation wavelength (expressed as a phase bias

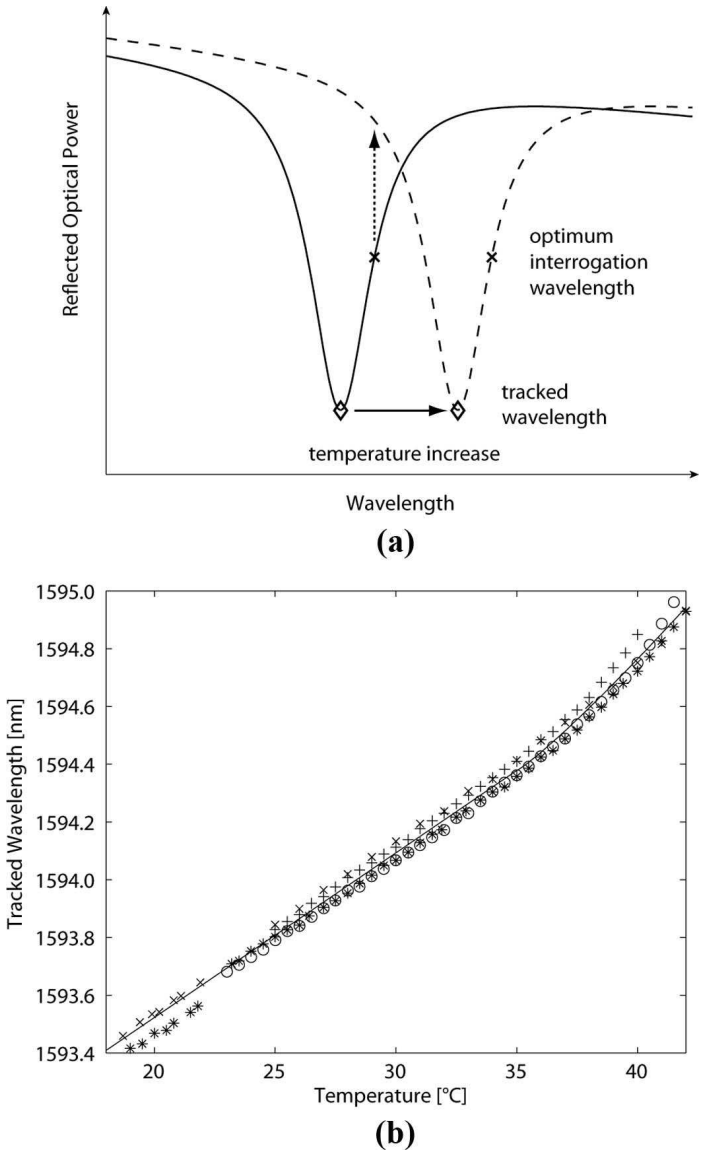

Fig. 2. Temperature measurement using a 7-μm high-finesse Fabry-Perot interferometer. (a) The tracked interference pattern showing the dip in reflected optical power at resonance, the optimum interrogation wavelength, and the tracked wavelength minimum. (b) Experimental calibration measurements showing the change in the tracked wavelength with temperature (each test is shown by a different marker).

term) is typically referred to as the interferometer transfer function.

Here, a planar 7-μm high-finesse Fabry-Perot interferometer made from 2 dichroic mirrors separated by a polymer film spacer was used. The sensor interrogation beam was provided by a 10-mW fiber-coupled tunable cw external cavity laser (ECL5000DT, Thorlabs, Inc., Newton, NJ). The scanning system and the sensor manufacture have both previously been described in detail by Zhang *et al.* [31]. For the 7-μm Fabry-Perot sensor, the effective element radius was approximately 25 μm (full width at half maximum) [32]. The selection of the optimum wavelength at each interrogation position (an automated process known as sensor pretuning) was completed by sweeping the laser wavelength through a range of 1585 to 1605 nm, recording the reflected optical power, and then determining the wavelength at the maximum value of the gradient [31]; see Fig. 2(a), the crosses illustrate the optimum interrogation wavelength. This procedure maximizes the sensitivity, linearity, and dynamic range of the sensor. Note that the optimum value could equally be chosen as the wavelength at the maximum negative value of the gradient.

C. Fabry-Perot Temperature Measurement

Because the power of the reflected optical signal is dependent on the optical thickness of the interferometer (dictated primarily by the physical distance between the parallel mirrors), any mechanism that modifies this parameter will also modify the detected signal. If the sensor is subject to a temperature increase, the polymer film spacer will expand, increasing the wavelength at which interference resonance occurs; see Fig. 2(a). For a fixed interrogation wavelength, this dependence can be used to recover temperature by monitoring the accompanying change in the reflected signal power; see, e.g., [33]. Recently, Morris *et al.* reported a technique in which both temperature and pressure could be recovered from a Fabry-Perot fiber-optic hydrophone [34], [35]. The temperature was extracted from low-frequency changes in the reflected optical power at the optimum interrogation wavelength based on an *a priori* calibration.

Here, a similar technique was used to make temperature-triggered ultrasound measurements with a planar Fabry-Perot polymer film interferometer. The procedure was as follows. First, the optimum wavelength was determined for each sensor interrogation position while at a stable temperature. The acquisition system was then started and the interference pattern at one of the interrogation positions periodically rescanned (typically the center point). Because it is only the interference region that is of interest, the rescanning wavelength sweep was reduced to a 5-nm range around the optimum wavelength. A Lorentzian function was fitted to the measured interference pattern and used to determine the wavelength at the minimum reflected power. A representative output is shown in Fig. 2(a); the diamonds illustrate the tracked minimum. The drift in the interference minimum was then used to correct the pretuned optimum wavelength values over the entire scan area. The absolute temperature value was also extracted from the tracked wavelength minimum, again based on an *a priori* calibration; see Fig. 2(b). The temperature value was then used to trigger ultrasonic measurements at certain temperature intervals (e.g., in a cooling fluid), or simply recorded when measurements were manually triggered. For a scan area containing 100 interrogation points, this method of temperature drift correction was approximately 2 orders of magnitude faster than repeating the optimum wavelength pretuning for all interrogation points. Provided the scan area is much smaller than the illumination beam width (i.e., there is no

temperature gradient across the scan area), it is valid to assume that the drift in the optimum wavelength is the same at each of the interrogation points.

This approach recovers the temperature by directly monitoring the drift of the resonant interference pattern, rather than temperature-induced changes in the reflected power (as used by Morris *et al.* [35]). The latter is considerably faster and allows simultaneous temperature measurement using a second data acquisition system. However, the former is potentially more robust, because the drift in the interference pattern is not influenced by other possible sources of variation in the reflected optical power (e.g., variations in the laser source strength or changes in the fiber alignment). For the current application, continuous measurement of the ultrasonic pressure is not required. Consequently, the same acquisition system can be used to make sequential measurements of temperature and pressure. Because the temperature is only monitored (and not controlled in any way), temperature-dependent measurement data can be obtained by first cooling or heating the test fluid. Temperature-triggered measurements can then be made as the fluid returns to room temperature. Similarly, for highly absorbing test fluids, the heating caused by ultrasonic absorption may be sufficient to increase the temperature gradually across the required range.

The temperature-wavelength calibration measurements for the 7-μm Fabry-Perot sensor are shown in Fig. 2(b). These were obtained by simultaneously tracking the wavelength at the interference minimum and the temperature at the sensor measurement surface as recorded by a 1-mm k-type thermocouple. Both heated (4 measurements) and cooled (2 measurements) distilled water was added to the measurement basin and allowed to return to room temperature. Between each measurement, the basin was detached and then replaced, mimicking the normal measurement procedure in which the basin is cleaned (see discussion in Section III-A). This procedure disturbs the absolute alignment between the interrogation laser and the Fabry-Perot interferometer. As a result, the same laser scanning position does not always point at the same physical location on the interferometer surface. This is the reason for the variation in the vertical offset of the curves shown in Fig. 2(b). The gradient, however, remains very robust. To account for this variation, a single-point temperature-wavelength calibration was repeated before each measurement to determine the vertical offset of the temperature-wavelength curve. The standard deviation in the recovered measurement at a stable temperature was less than 0.05°C, making the accuracy primarily dependent on the thermocouple used for the calibration. This yields a temperature measurement accuracy of ± 0.35°C. Although it is possible to monitor the temperature directly during a transmission measurement using a thermocouple, at higher frequencies, even a small thermocouple junction will disturb the wave path. Because the drift in the resonant interference pattern must be monitored in any case (to maintain the sensitivity of the sensor), it is straightforward to also use the sensor for accurate *in situ* temperature measurements.

III. Experimental Method

A. Experimental Measurement Procedure

The laser and optical absorber arrangement described in Section II-A, herein the "source," was positioned within a small plastic basin fitted with the Fabry-Perot sensor (see Fig. 1). The fluid volume was always controlled such that the black absorbent layer was completely submerged but the upper side of the substrate was not within the fluid. This was done to prevent variation in the illumination fluence-rate caused by optical absorption within the fluid. The vertical placement of the source was controlled via a translation stage allowing 2 cm of calibrated movement. Coarse adjustments were also possible via the post-and-connector assembly joining the source to the bench. The planar alignment of the source and the Fabry-Perot sensor was controlled via a double-tilt stage connected between the aluminum source housing and the translation stage.

For each measurement, the source was first positioned within the basin at the desired measurement distance (typically 6.5 mm). The planar alignment was approximately adjusted, and the basin was then filled with distilled water (the reference fluid) as illustrated in Fig. 1. Next, a single temperature-wavelength calibration measurement was completed, and the desired temperature triggers entered into the acquisition system. The source was then switched on[1] and 10-mm line scans about the sensor origin used to refine the planar alignment of the source and sensor via the double tilt stage. These scans were also used to identify the possible presence of air bubbles and any other illumination or alignment problems. After this preliminary measurement and adjustment, the pretuning procedure was completed to determine the optimum interrogation wavelength at each of the scan positions. This was done with the source switched off and the fluid at a stable temperature. The temperature-tracking acquisition software was then started, and several transmission measurements manually triggered in the distilled water. The water was then removed from the basin using a syringe and thin plastic tubing without modifying the source to sensor distance or alignment. Next, the test fluid was added to the basin and the required temperature (or manually) triggered measurements taken. Finally, the basin was removed, the fluid discarded, and the basin and source cleaned. The complete procedure was repeated several times for each test fluid of interest. The reference measurements were repeated for each test because the removal of the basin and the cleaning of the source disturbed the alignment between the source and sensor.

For the measurements presented here, a centered 10 × 10 grid of scan points was used (500 × 500 μm with a 50-μm step size). The small scan area was chosen so the

[1]Both the interrogation and source lasers were first allowed to warm up and then left running continuously. The photoacoustic source was controlled by adding and removing a black metal wedge placed between the fiber tip and the PMMA absorber.

assumption of a planar incident wave remained valid. A scan area was used (rather than multiple acquisitions at a single point) to prevent the focused interrogation laser from continuously illuminating the same sensor position at a high repetition frequency, which may lead to local heating. The signal-to-noise ratio of the measurement was improved through spatial averaging. Care was taken to select a step size larger than the effective spot radius of the sensor. During the measurement procedure, the drift in the interference minimum was continually monitored (with a sampling frequency of 0.6 Hz) until an ultrasonic measurement was triggered. The signal at each point on the scan grid was then recorded sequentially, with the measurement acquisitions individually triggered by a photodiode positioned near the output of the source excitation laser. The signals were acquired at a sampling frequency of 2.5 GHz using a sample length of 10 μs (25 000 samples). To minimize the scan time, no temporal averaging was used. The utilized sensor interrogation wavelengths were calculated using the initial pretuning values offset by the most recent value for the drift in the interference minimum. Each ultrasonic measurement took approximately 5 s, after which the temperature drift measurements were resumed and the procedure continued until all the measurements were complete.

B. Signal Analysis

To extract the ultrasonic attenuation and dispersion data, the recorded impulse response signals were processed as follows. First, the reference and test data files (from the same test) were loaded and each spatially averaged to give a pair of time-domain impulse signals. The time between the laser trigger and the maximum arrival peak in the reference impulse was used in conjunction with the known temperature-dependent speed of sound in distilled water (computed using the 5th order polynomial given by Marczak [36]) to calculate the precise source to sensor distance d. The nominal speed of sound in the test fluid $c_{\text{test fluid}}$ was then calculated using this distance and the time between the laser trigger and the maximum arrival peak in the test impulse. Next, the time-domain impulse signals were symmetrically truncated (around their maximum arrival peak) to 2048 samples and windowed using a Hanning window. The shortened signals were circular shifted so that the peak of each impulse coincided with the beginning of the signal. This was to remove the linear part of the phase [37], [38]. The single-sided amplitude and phase spectrums were then computed via a 4096-point (zero-padded) fast Fourier transform.

The propagation of a plane wave $e^{i\underset{\sim}{k}(f)d}$ in an attenuating and dispersive medium can be modeled using a complex wave number of the form $\underset{\sim}{k}(f) = 2\pi f/c(f) + i\alpha(f)$ [39], [40]. This yields a decaying frequency-dependent amplitude term $e^{-\alpha(f)d}$. The attenuation coefficient $\alpha(f)$ in decibels per centimeter can be recovered via the amplitude spectrum ratio

$$\alpha_{\text{test fluid}}(f) = -\frac{8.686}{d}\ln\left[\frac{A_{\text{test fluid}}(f)}{A_{\text{water}}(f)}\right] + \alpha_{\text{water}}(f), \tag{1}$$

where $A_{\text{test fluid}}$ and A_{water} are the measured single-sided amplitude spectrums, d is the source to sensor distance in centimeters, and $\alpha_{\text{water}}(f)$ is the attenuation in water in decibels per centimeter. The latter was calculated here using a 7th-order polynomial fitted to the experimental data provided by Pinkerton [41]. The frequency-dependent sound speed $c(f)$ in meters per second can similarly be recovered from the single-sided phase spectrums

$$c(f) = \frac{c_{\text{test fluid}}}{1 - c_{\text{test fluid}}\frac{\phi_{\text{test fluid}}(f) - \phi_{\text{water}}(f)}{2\pi f d}}, \tag{2}$$

where $\phi_{\text{test fluid}}$ and ϕ_{water} are the measured test spectrums, and d must be converted to meters [40]. Note that the equation given here uses the nominal sound speed in the test fluid (rather than the reference fluid). This is because the truncated time windows are taken symmetrically about the individual data peaks (see discussion in Section III-B). The use of $c_{\text{test fluid}}$, which is dependent on the location of these peaks, rather than c_{water} restores the phase component associated with this offset. It is also useful to note that the required parameters could similarly be extracted from 2 measurements in the same test fluid at different source-to-sensor distances. This would eliminate the need for knowing the attenuation properties of the reference fluid *a priori*. However, as the attenuation in distilled water is less than most test fluids of biological interest (and significantly less than the oils used as test fluids in the current study), its use as a reference allows the measurement bandwidth to be increased (the signal-to-noise of the amplitude ratio is improved).

C. System Characterization

An example of the spatially averaged time-domain impulse signals recorded in distilled water and olive oil at 25°C is shown in Fig. 3(a). The impulse in olive oil has been considerably attenuated and arrives later because of the lower sound speed in the fluid. The corresponding single-sided amplitude spectrums are shown in Fig. 3(b). The upper curve in Fig. 3(b) illustrates the frequency response of the source and sensor after correction for attenuation in water (computed using the extracted source to sensor distance and the attenuation data from Pinkerton [41]). This gives a combined −6-dB bandwidth for the source and sensor of 1 to 35 MHz. It is useful to note that the relative signal level in the corrected spectrum is still −10 dB at 100 MHz (approximately 25 dB above the noise floor). The calculated −3-dB bandwidth for the 7-μm Fabry-Perot sensor alone is 122 MHz (based on an experimentally validated model of frequency response [42]; the

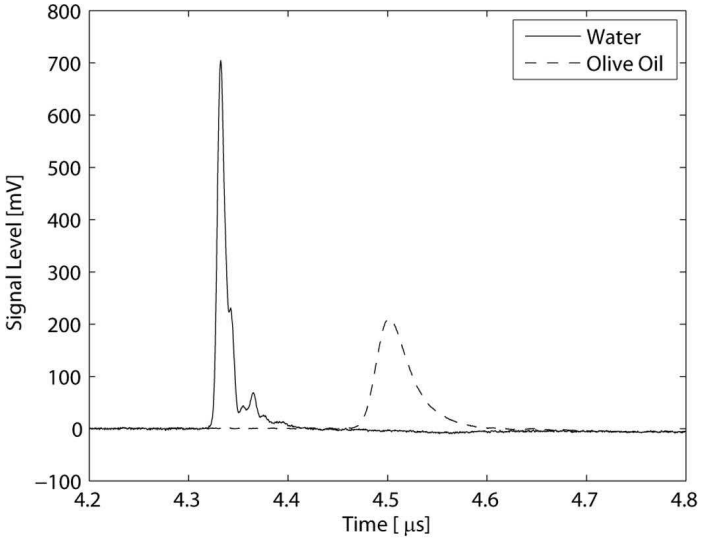

(a)

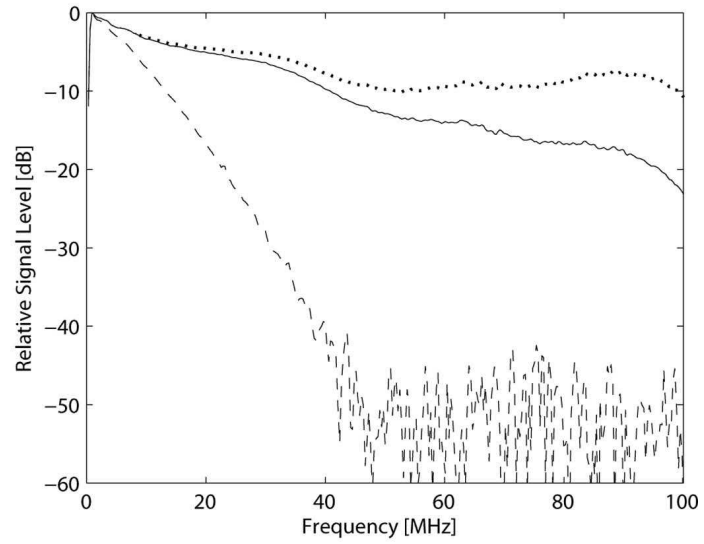

(b)

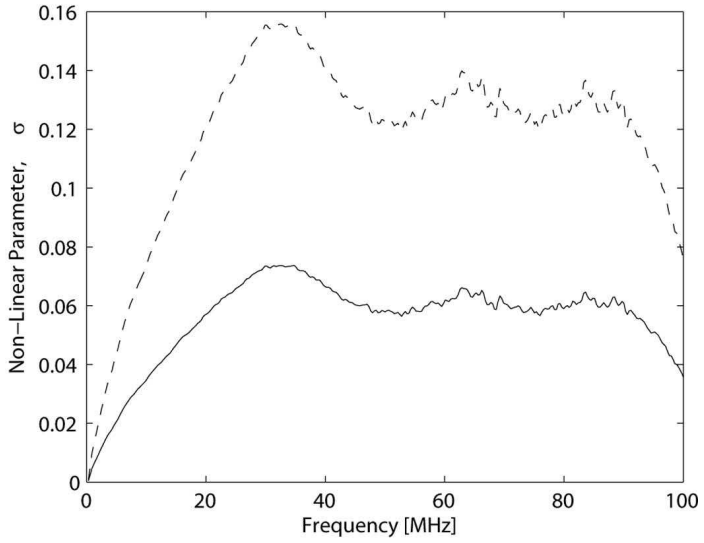

(c)

Fig. 3. (a) Captured time domain impulse signals in distilled water (solid line) and olive oil (dashed line) at 25°C, (b) the corresponding frequency spectrums where the dotted line is the spectrum in water including correction for attenuation, and (c) the nonlinear (shock) parameter in distilled water and olive oil.

−3-dB bandwidth for the photodiode detector extends to 200 MHz). The bandwidth of the source is limited by the pulse duration of the source excitation laser (in this case, 5.6 ns). Variation in the thickness of the source paint layer had only a small effect on the bandwidth, with an increase in thickness gradually reducing the high-frequency components caused by ultrasonic absorption within the paint layer itself [24]. For biological and phantom materials with weak ultrasonic attenuation (e.g., blood and intralipid), the system facilitates very wideband measurements covering both the traditional diagnostic and high-frequency spectrums. The nonlinear shock parameter calculated for both water and olive oil is shown in Fig. 3(c). This was calculated using the relationship

$$\sigma = \frac{\beta p_0 2\pi f d}{\rho_0 {c_0}^3}, \tag{3}$$

as defined by Szabo [43]. Here $\beta = 1 + B/2A$ is the coefficient of nonlinearity (approximately 6 in olive oil and 3.5 in water), p_0 is the source pressure, f is the frequency, ρ_0 is the density, c_0 is the sound speed, and d is the propagation distance (all in standard SI units). Because shock formation does not occur until $\sigma = 1$, the measurement system remains within linear operating conditions.

IV. Experimental Measurement of Power Law Attenuation

A. Extraction of Power Law Parameters

It is well known that the ultrasonic attenuation of a plane wave in a wide variety of propagation media (including most fluids and biological tissues) can be described by a frequency power law of the form

$$\alpha(f) = \alpha_0 f^{\,y}, \tag{4}$$

(e.g., [44]). Here α is the attenuation in decibels per centimeter, and f is the frequency in megahertz. The dependence of attenuation on frequency brings with it a dissipative dispersion (i.e., a dependence of the phase velocity on frequency) that is required by causality [39]. For media in which the attenuation obeys a frequency power law, this dispersion can be calculated using the Kramers-Krönig relations described by Waters *et al.* [40] (note that these relationships ensure absolute rather than relativistic causality). For $1 < y < 3$, the appropriate dispersion relation is given by

$$c(f) = \left[\frac{1}{c_0} + \hat{\alpha}_0 \tan\left(\frac{\pi y}{2}\right)\left(|\omega|^{y-1} - |\omega_0|^{y-1}\right)\right]^{-1}, \tag{5}$$

where the dispersion is given as a variation from a known sound speed c_0 at a particular frequency ω_0, ω and ω_0 are in radians per second, and $\hat{\alpha}_0$ is calculated by

$$\hat{\alpha}_0 = \frac{100\alpha_0}{8.686}\left(\frac{10^{-6}}{2\pi}\right)^y. \quad (6)$$

This conversion is required because (4) is based on a power law relationship of the form $\hat{\alpha} = \hat{\alpha}_0\omega^y$ with $\hat{\alpha}$ in Nepers per meter and ω in radians per second.

The signal analysis procedure described in Section III-B results in test measurements at a range of temperatures being processed relative to a reference measurement at a single temperature. This ignores any variation of the source efficiency (i.e., the Grüneisen parameter) with temperature. Consequently, the uncorrected attenuation curves display a systematically decreasing vertical intercept (the source efficiency gradually increases with temperature). Similarly, any variation in the transmission coefficient from the source to the reference and test fluids is also ignored. To account for these variations, a power law of the form

$$\alpha(f) = \alpha_0 f^y + \alpha_1, \quad (7)$$

was used instead of (4). This typically yielded α_1 values on the order of $\pm$ 1 dB that linearly decreased with temperature. It is usually assumed that the DC component of the attenuation is negligible [43], [44], in which case the fitting parameter α_1 can be taken as the relative source efficiency between the test fluid at a particular temperature and the reference fluid.

To obtain the power law parameters, (7) and (5) were simultaneously fitted to the experimental attenuation and sound speed data, calculated using (1) and (2), respectively, using an unconstrained nonlinear optimization (fminsearch in MATLAB, R2008a, MathWorks, Inc., Natick, MA). This approach improved the accuracy and robustness of the fitting procedure because both amplitude and phase information were explicitly considered. Previously, power law parameters have been obtained from measured attenuation data, with dispersion data used to prove the applicability of the Kramers-Kronig relationships [40], [45]. Note that the parameters c_0 and ω_0 in (5) were obtained from the sound speed and frequency at the center of the fit range.

B. Power Law Attenuation in Oils

To illustrate the efficacy of the measurement system, the temperature-dependent attenuation and dispersion were measured in 2 test fluids; castor oil (Sigma-Aldrich 18722) and olive oil (O1514, Sigma-Aldrich, St. Louis, MO). Both are readily available, and sufficient reference data already exist, particularly for castor oil. Each fluid was tested 4 times, with the fluid cooled to 15°C before being added to the measurement basin. The corresponding temperature rise in the test fluids (from 18°C) under constant insonification in normal test conditions is shown in Fig. 4. The nominal source-to-sensor distance was 6.4 mm, and the ambient room temperature 23.5°C. The

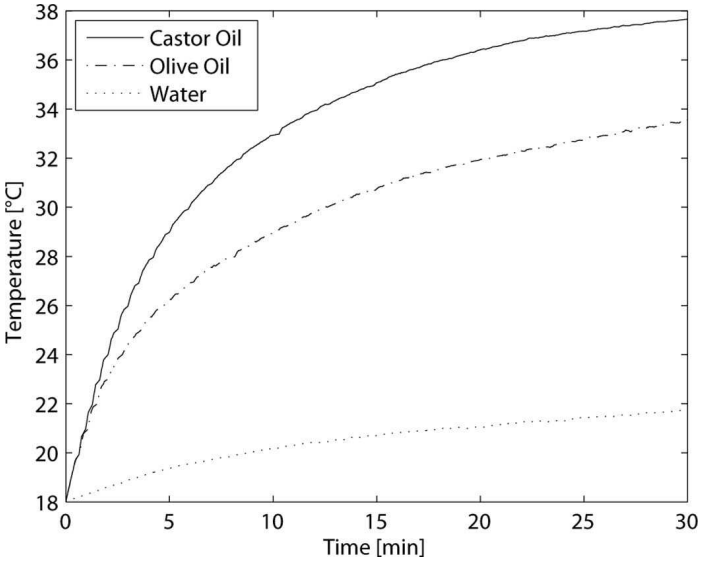

Fig. 4. Temperature rise in cooled test fluids caused by ultrasonic attenuation.

ultrasonic attenuation in both test fluids was sufficient to increase the fluid temperature gradually to a reasonably high equilibrium. The small temperature change evident in the distilled water suggests that the majority of this temperature increase was due to absorption, rather than heating via the black optical absorber. Measurements were triggered from 20°C at 1°C intervals until a stable temperature was reached (39°C in castor oil, 34°C in olive oil). For the current investigation, this range of temperatures was considered sufficient. However, measurements covering a wider range could easily be obtained by further cooling or heating the test fluids before measurement. This is particularly relevant for less absorbing test fluids, where a wide temperature range may be obtained by using both heated and cooled fluid, and triggering measurements as the temperature stabilizes.

The extracted power law parameters for castor oil are shown in Fig. 5(a) and (b). The circles and error bars illustrate the mean and standard deviation across the 4 measurements. The fits were obtained using the data from 2 to 20 MHz (for a particular test fluid, the bandwidth of the useful measurement data is determined by the magnitude of the attenuation in the test fluid; castor oil is highly absorbing, thus, the bandwidth is reduced). The attenuation decreases with increasing temperature because of a decrease in viscosity [46], [47]. This is reflected in the significant decrease in the power law coefficient α_0. There is also a gradual increase in the power law exponent with temperature, consistent with previous measurement data. For example, Tong and Povey [38] reported an increase in the exponent from 1.66 to 1.74 over the temperature range 20 to 35°C (measured in 5° increments over 2 to 8 MHz). Power law exponents ranging from 1.57 (measured at 19.4°C over 2 to 10 MHz [48]) to 1.77 (measured at 30° over 1 to 5 MHz [49]) have also previously been reported, with 1.66 or 1.67 the most commonly reported value at 20°C [38], [45], [50]–[52]. The variation in the recorded

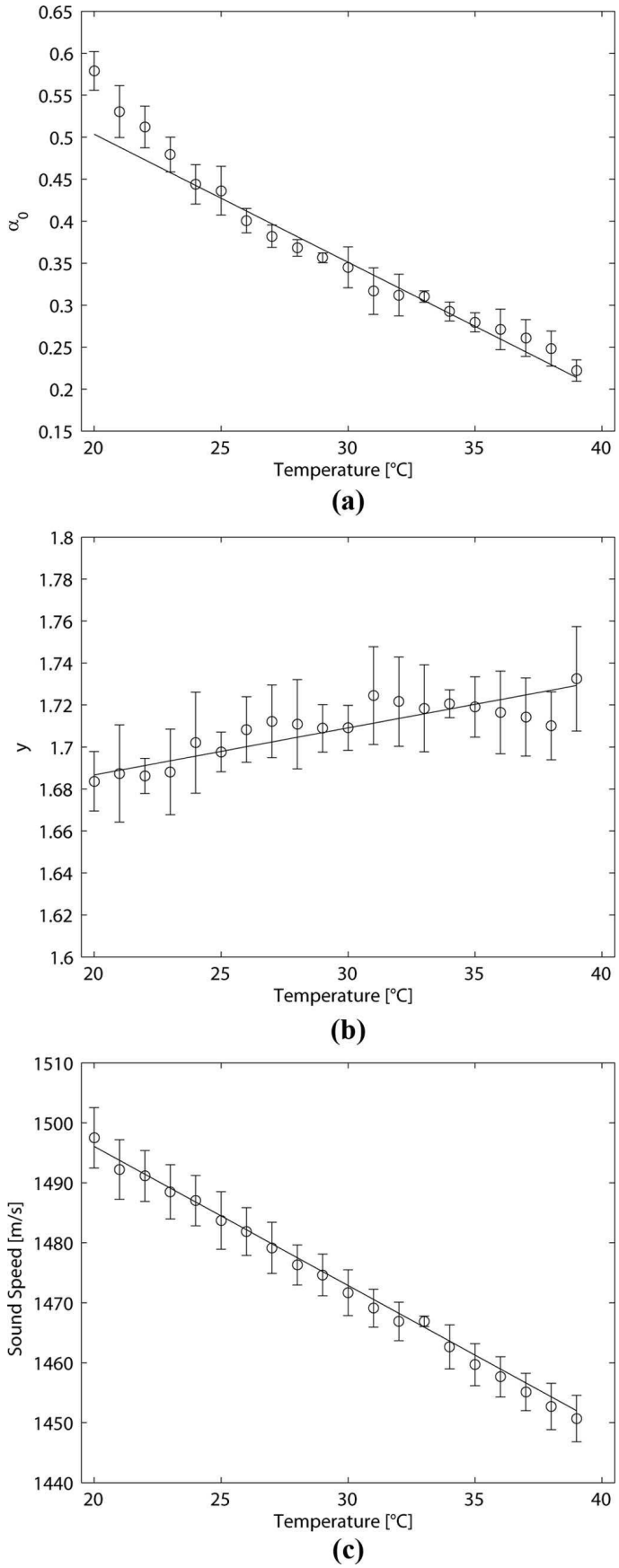

Fig. 5. Experimental measurements for the ultrasonic attenuation and sound speed in castor oil; (a) power law coefficient α_0, (b) power law exponent y, and (c) nominal sound speed. The circles and error bars illustrate the mean and standard deviation of the experimental results, and the solid lines are weighted linear fits.

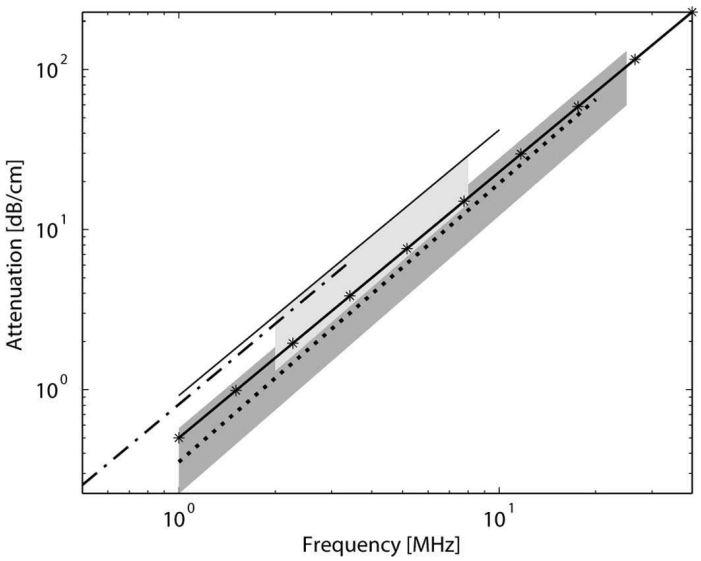

Fig. 6. Comparison of selected attenuation measurements in castor oil from the literature. Solid line: 20°C [51], dash-dot line: 20°C [52], solid line and stars: 30°C [50], dotted line: 37°C [40], light shaded area: 20–35°C [38], and dark shaded area: 20–39°C (current measurements).

values can be attributed to the myriad of experimental techniques, the differences in the fitted frequency range, and variations in the composition of the castor oil itself. A comparison between the current results and selected castor oil attenuation measurements from the literature is given in Fig. 6. The offset between the results presented by Tong and Povey (light-gray shaded area) and the current measurements (dark-gray shaded area) can be explained by the systematically higher sound speeds reported in the former. This suggests an increased oil density and, consequently, higher values of attenuation. The nominal sound speed measured here is shown in Fig. 5(c). The analogous results for olive oil are shown in Fig. 7, where the fits were obtained using the data from 2 to 35 MHz. Again, a decrease in attenuation with increasing temperature is evident because of a decrease in viscosity. The dispersion values for both oils can be recovered using the reported power law parameters and the Kramers-Krönig relation given in (5).

V. Discussion and Conclusion

The development of high-resolution imaging modalities based on ultrasonic wave propagation relies on an understanding of the ultrasonic properties of the materials under investigation. This is particularly true for techniques that attempt to extract quantitative diagnostic information. To obtain higher resolution images, higher ultrasonic frequencies must invariably be used. The substantial ultrasonic attenuation in biological tissues at these frequencies then becomes an important factor in the data extraction. PAT, as one example of a high-resolution ultrasonic imaging modality, has shown particular promise for the *in vivo* visualization of vascular structures [53]. Images are produced by irradiating the skin with short pulses of

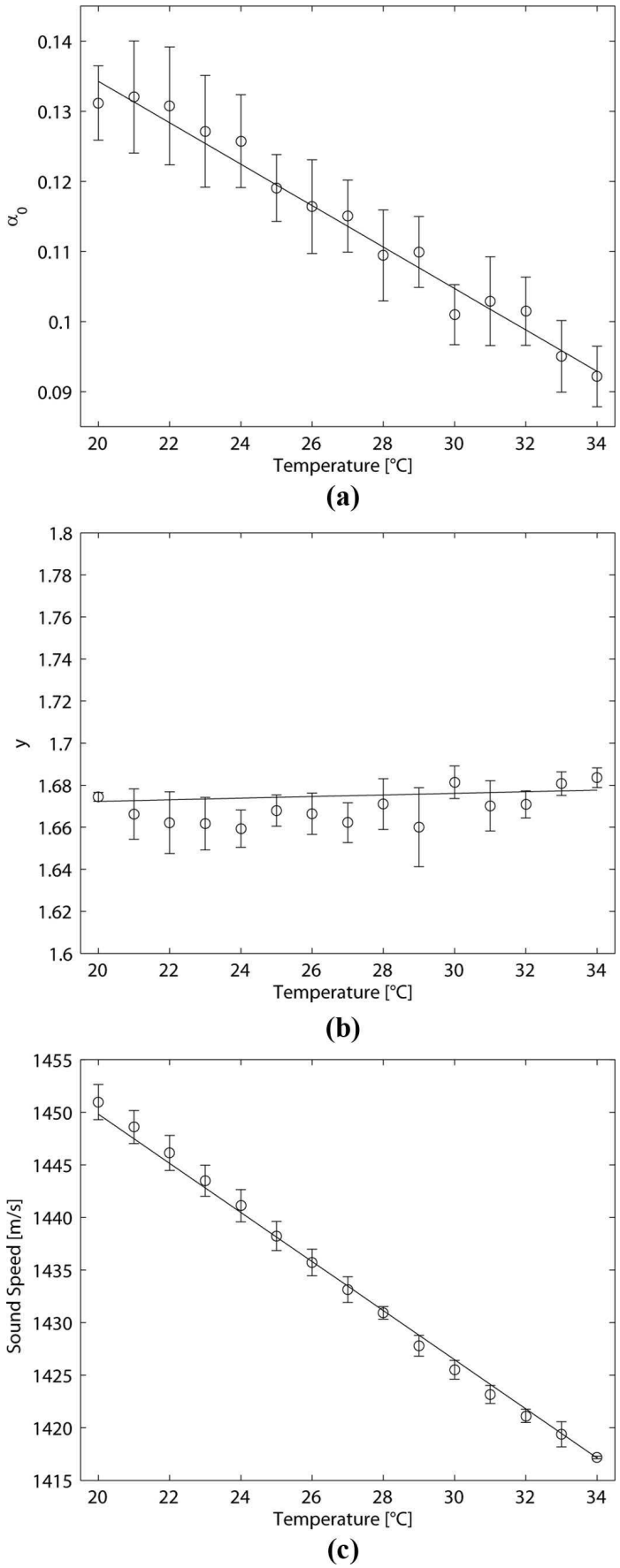

Fig. 7. Experimental measurements for the ultrasonic attenuation and sound speed in olive oil; (a) power law coefficient α_0, (b) power law exponent y, and (c) nominal sound speed. The circles and error bars illustrate the mean and standard deviation of the experimental results, and the solid lines are weighted linear fits.

laser light. The localized absorption of this light within the tissue then generates broadband ultrasonic waves via thermoelastic expansion. These propagate back to the surface where they are detected. Using simple models of ultrasound propagation, qualitative images of the absorbed energy distribution can be obtained, and thus a picture of the vascular structure is produced. However, the extraction of quantitative data relies on the accurate modeling of the ultrasonic wave propagation in tissue. It is usually assumed that the propagation medium is acoustically homogeneous and nonabsorbing. The accurate quantification of the ultrasonic properties of the vasculature and tissue structures under investigation (covering both the high-frequency and traditional diagnostic spectrum) is thus important for the continued development of the modality. The same conditions apply for high-frequency pulse-echo type ultrasound, where the application specific characterization of many materials is still required.

Here, a photoacoustic technique for the broadband measurement of temperature-dependent ultrasonic attenuation and dispersion has been described. This uses existing high bandwidth optical source-and-receiver technologies to make transmission ultrasound measurements of attenuation, dispersion, and sound speed. The Fabry-Perot sensor system is extended to make direct measurements of the sample temperature at the sensor surface. This is particularly important for the accurate characterization of materials at both *in vivo* and *in vitro* temperatures. For biological materials with relatively low ultrasonic attenuation (e.g., blood), the system permits broadband measurements covering both the traditional diagnostic and high-frequency spectrums. Indeed, it is the magnitude of the ultrasonic attenuation of the tested material that ultimately dictates the useful bandwidth of the system. However, even in highly absorbing fluids (e.g., castor oil), broadband measurements up to 20 MHz are still possible. Although this bandwidth may be further increased by decreasing the source-to-sensor distance, for some biological materials, thin sample layers may no longer be representative of the overall material structure. To illustrate the efficacy of the system, the temperature-dependent power law parameters and sound speed in 2 reference fluids are presented. These results are consistent with previous experiments reported in the literature. Although the measurement system is primarily discussed in relation to fluids, the same technique could equally be used for the study of other materials. It is planned to use the developed system for the broadband ultrasonic characterization of biological tissues and fluids relevant to PAT.

References

[1] F. A. Duck, *Physical Properties of Tissue: A Comprehensive Reference Book*. London: Academic Press, 1990.

[2] J. C. Bamber, "Ultrasonic properties of tissue," in *Ultrasound in Medicine*, F. A. Duck, A. C. Baker, and H. C. Starritt, Eds. London: Institute of Physics Publishing, 1998, pp. 57–88.

[3] P. N. T. Wells, "Ultrasonic imaging of the human body," *Rep. Prog. Phys.*, vol. 62, no. 5, pp. 671–722, 1999.

[4] D. I. Hughes and F. A. Duck, "Automatic attenuation compensation for ultrasonic imaging," *Ultrasound Med. Biol.*, vol. 23, no. 5, pp. 651–664, 1997.

[5] G. R. Lockwood, D. H. Turnball, D. A. Christopher, and F. S. Foster, "Beyond 30 MHz [Applications of high-frequency ultrasound imaging]," *IEEE Eng. Med. Biol. Mag.*, vol. 15, no. 6, pp. 60–71, 1996.

[6] F. S. Foster, C. J. Pavlin, K. A. Harasiewicz, D. A. Christopher, and D. H. Turnbull, "Advances in ultrasound biomicroscopy," *Ultrasound Med. Biol.*, vol. 26, no. 1, pp. 1–27, 2000.

[7] S. El Gammal, C. El Gammal, K. Kaspar, C. Pieck, P. Altmeyer, M. Vogt, and H. Ermert, "Sonography of the skin at 100 MHz enables *in vivo* visualization of stratum corneum and viable epidermis in palmar skin and psoriatic plaques," *J. Invest. Dermatol.*, vol. 113, no. 5, pp. 821–829, 1999.

[8] E. Ruocco, G. Argenziano, G. Pellacani, and S. Seidenari, "Noninvasive imaging of skin tumors," *Dermatol. Surg.*, vol. 30, pp. 301–310, Feb. 2004.

[9] C. Passmann and H. Ermert, "A 100-MHz ultrasound imaging system for dermatologic and ophthalmologic diagnostics," *IEEE Trans. Ultrason. Ferroelectr. Freq. Control*, vol. 43, no. 4, pp. 545–552, Jul. 1996.

[10] M. Xu and L. V. Wang, "Photoacoustic imaging in biomedicine," *Rev. Sci. Instrum.*, vol. 77, no. 4, art. no. 041101, 2006.

[11] L. Pan, L. Zan, and F. S. Foster, "Ultrasonic and viscoelastic properties of skin under transverse mechanical stress *in vitro*," *Ultrasound Med. Biol.*, vol. 24, no. 7, pp. 995–1007, Sep. 1998.

[12] S. G. Ye, K. A. Harasiewicz, C. J. Pavlin, and F. S. Foster, "Ultrasound characterization of normal ocular tissue in the frequency range from 50 MHz to 100 MHz," *IEEE Trans. Ultrason. Ferroelectr. Freq. Control*, vol. 42, no. 1, pp. 8–14, Jan. 1995.

[13] G. R. Lockwood, L. K. Ryan, J. W. Hunt, and F. S. Foster, "Measurement of the ultrasonic properties of vascular tissues and blood from 35–65 MHz," *Ultrasound Med. Biol.*, vol. 17, no. 7, pp. 653–666, 1991.

[14] T. A. Whittingham, "Broadband transducers," *Eur. Radiol.*, vol. 9, Suppl. 3, pp. S298–S303, 1999.

[15] J. Kuskibiki, N. Akashi, T. Sannomiya, N. Chubachi, and F. Dunn, "VHF/UHF range bioultrasonic spectroscopy system and method," *IEEE Trans. Ultrason. Ferroelectr. Freq. Control*, vol. 42, no. 6, pp. 1028–1039, Nov. 1995.

[16] P. J. La Rivière, J. Zhang, and M. A. Anastasio, "Image reconstruction in optoacoustic tomography for dispersive acoustic media," *Opt. Lett.*, vol. 31, no. 6, pp. 781–783, Mar. 2006.

[17] B. E. Treeby and B. T. Cox, "Fast, tissue-realistic models of photoacoustic wave propagation for homogeneous attenuating media," *Proc. SPIE*, vol. 7177, art. no. 717716, 2009.

[18] B. T. Cox, S. Kara, S. R. Arridge, and P. C. Beard, "k-space propagation models for acoustically heterogeneous media: Application to biomedical photoacoustics," *J. Acoust. Soc. Am.*, vol. 121, no. 6, pp. 3453–3464, Jun. 2007.

[19] J. Laufer, D. Delpy, C. Elwell, and P. Beard, "Quantitative spatially resolved measurement of tissue chromophore concentrations using photoacoustic spectroscopy: Application to the measurement of blood oxygenation and haemoglobin concentration," *Phys. Med. Biol.*, vol. 52, no. 1, pp. 141–168, Jan. 2007.

[20] J. Laufer, C. Elwell, D. Delpy, and P. Beard, "*In vitro* measurements of absolute blood oxygen saturation using pulsed near-infrared photoacoustic spectroscopy: Accuracy and resolution," *Phys. Med. Biol.*, vol. 50, no. 18, p. 4409–4428, 2005.

[21] R. T. Towa, R. J. Miller, L. A. Frizzell, J. F. Zachary, and W. D. O'Brien Jr., "Attenuation coefficient and propagation speed estimates of rat and pig intercostal tissue as a function of temperature," *IEEE Trans. Ultrason. Ferroelectr. Freq. Control*, vol. 49, no. 10, pp. 1411–1420, Oct. 2002.

[22] R. J. von Gutfeld and R. L. Melcher, "20-MHz acoustic waves from pulsed thermoelastic expansions of constrained surfaces," *Appl. Phys. Lett.*, vol. 30, no. 6, pp. 257–259, 1977.

[23] A. Meyer, S. Gspan, S. Bernet, and M. Ritsch-Marte, "Binary optoacoustic holography with a spatial light modulator," *J. Appl. Phys.*, vol. 96, no. 10, pp. 5886–5891, 2004.

[24] Y. Hou, S. Ashkenazi, H. Sheng-Wen, and M. O'Donnell, "Improvements in optical generation of high-frequency ultrasound," *IEEE Trans. Ultrason. Ferroelectr. Freq. Control*, vol. 54, no. 3, pp. 682–686, Mar. 2007.

[25] G. C. Wetsel Jr., "Photothermal generation of thermoelastic waves in composite media," *IEEE Trans. Ultrason. Ferroelectr. Freq. Control*, vol. 33, no. 5, pp. 450–461, Sep. 1986.

[26] C. G. A. Hoelen and F. F. M. de Mul, "A new theoretical approach to photoacoustic signal generation," *J. Acoust. Soc. Am.*, vol. 106, no. 2, pp. 695–706, 1999.

[27] B. T. Cox and P. C. Beard, "Fast calculation of pulsed photoacoustic fields in fluids using k-space methods," *J. Acoust. Soc. Am.*, vol. 177, no. 6, pp. 3616–3627, 2005.

[28] P. C. Beard, "Two-dimensional ultrasound receive array using an angle-tuned Fabry-Perot polymer film sensor for transducer field characterization and transmission ultrasound imaging," *IEEE Trans. Ultrason. Ferroelectr. Freq. Control*, vol. 52, no. 6, pp. 1002–1012, Jun. 2005.

[29] E. Zhang and P. Beard, "Broadband ultrasound field mapping system using a wavelength tuned, optically scanned focused laser beam to address a Fabry Perot polymer film sensor," *IEEE Trans. Ultrason. Ferroelectr. Freq. Control*, vol. 53, no. 7, pp. 1330–1338, Jul. 2006.

[30] Y. Hou, J. S. Kim, H. Sheng-Wen, S. Ashkenazi, L. J. Guo, and M. O'Donnell, "Characterization of a broadband all-optical ultrasound transducer—From optical and acoustical properties to imaging," *IEEE Trans. Ultrason. Ferroelectr. Freq. Control*, vol. 55, no. 8, pp. 1867–1877, Aug. 2008.

[31] E. Zhang, J. G. Laufer, and P. C. Beard, "Backward-mode multiwavelength photoacoustic scanner using a planar Fabry-Perot polymer film ultrasound sensor for high-resolution three-dimensional imaging of biological tissues," *Appl. Opt.*, vol. 47, no. 4, pp. 561–577, Feb. 2008.

[32] B. T. Cox and P. C. Beard, "The frequency-dependent directivity of a planar Fabry-Perot polymer film ultrasound sensor," *IEEE Trans. Ultrason. Ferroelectr. Freq. Control*, vol. 54, no. 2, pp. 394–404, Feb. 2007.

[33] X. Wan and H. F. Taylor, "Intrinsic fiber Fabry-Perot temperature sensor with fiber Bragg grating mirrors," *Opt. Lett.*, vol. 27, no. 16, pp. 1388–1390, Aug. 2002.

[34] P. Morris, A. Hurrell, E. Zhang, R. Srinath, and P. Beard, "A Fabry-Perot fibre-optic hydrophone for the measurement of ultrasound induced temperature change," in *Proc. IEEE Ultrasonics Symp.*, 2006, pp. 536–539.

[35] P. Morris, A. Hurrell, A. Shaw, E. Zhang, and P. Beard, "A Fabry-Perot fibre-optic ultrasonic hydrophone for the simultaneous measurement of temperature and acoustic pressure," *J. Acoust. Soc. Am.*, vol. 125, no. 6, pp. 3611–3623, 2009.

[36] W. Marczak, "Water as a standard in the measurements of speed of sound in liquids," *J. Acoust. Soc. Am.*, vol. 102, no. 5, pp. 2776–2779, 1997.

[37] S. I. Rokhlin, D. K. Lewis, K. F. Graff, and L. Adler, "Real-time study of frequency dependence of attenuation and velocity of ultrasonic waves during the curing reaction of epoxy resin," *J. Acoust. Soc. Am.*, vol. 79, no. 6, pp. 1786–1793, 1986.

[38] J. Tong and M. J. W. Povey, "Pulse echo comparison method with FSUPER to measure velocity dispersion in n-tetradecane in water emulsions," *Ultrasonics*, vol. 40, no. 1–8, pp. 37–41, 2002.

[39] W. Sachse and Y.-H. Pao, "On the determination of phase and group velocities of dispersive waves in solids," *J. Appl. Phys.*, vol. 49, no. 8, pp. 4320–4327, 1978.

[40] K. R. Waters, M. S. Hughes, J. Mobley, G. H. Brandenburger, and J. G. Miller, "On the applicability of Kramers-Krönig relations for ultrasonic attenuation obeying a frequency power law," *J. Acoust. Soc. Am.*, vol. 108, no. 2, pp. 556–563, Aug. 2000.

[41] J. M. M. Pinkerton, "The absorption of ultrasonic waves in liquids and its relation to molecular constitution," *Proc. Phys. Soc. B*, vol. 62, no. 2, pp. 129–141, 1949.

[42] P. C. Beard, F. Perennes, and T. N. Mills, "Transduction mechanisms of the Fabry-Perot polymer film sensing concept for wideband ultrasound detection," *IEEE Trans. Ultrason. Ferroelectr. Freq. Control*, vol. 46, no. 6, pp. 1575–1582, Nov. 1999.

[43] T. L. Szabo, *Diagnostic Ultrasound Imaging*. London: Elsevier Academic Press, 2004.

[44] T. L. Szabo, "Time domain wave equations for lossy media obeying a frequency power law," *J. Acoust. Soc. Am.*, vol. 96, no. 1, pp. 491–500, 1994.

[45] P. He, "Experimental verification of models for determining dispersion from attenuation," *IEEE Trans. Ultrason. Ferroelectr. Freq. Control*, vol. 46, no. 3, pp. 706–714, May 1999.

[46] H.-L. Kuo, "Variation of ultrasonic velocity and absorption with temperature and frequency in high viscosity vegetable oils," *Jpn. J. Appl. Phys.*, vol. 10, no. 2, pp. 167–170, 1971.

[47] E. E. Franco, J. C. Adamowski, R. T. Higuti, and F. Buiochi, "Viscosity measurement of Newtonian liquids using the complex reflec-

tion coefficient," *IEEE Trans. Ultrason. Ferroelectr. Freq. Control*, vol. 55, no. 10, pp. 2247–2253, Oct. 2008.

[48] N. Gladwell, C. Javanaud, K. Peers, and R. Rahalkar, "Ultrasonic behavior of edible oils: Correlation with rheology," *J. Am. Oil Chem. Soc.*, vol. 62, no. 8, pp. 1231–1236, 1985.

[49] G. R. Harris, B. A. Herman, S. W. Smith, and W. J. Bodine, Jr., "Through transmission technique for ultrasonic attenuation measurement using broadband plane wave pulses," in *Proc. Ultrasonics Symp.*, 1983, pp. 778–781.

[50] F. Dunn and J. E. Breyer, "Generation and detection of ultra-high-frequency sound in liquids," *J. Acoust. Soc. Am.*, vol. 34, no. 6, pp. 775–778, 1962.

[51] T. L. Szabo, "Causal theories and data for acoustic attenuation obeying a frequency power law," *J. Acoust. Soc. Am.*, vol. 97, no. 1, pp. 14–24, 1995.

[52] M. Liebler, S. Ginter, T. Dreyer, and R. E. Riedlinger, "Full wave modeling of therapeutic ultrasound: Efficient time-domain implementation of the frequency power-law attenuation," *J. Acoust. Soc. Am.*, vol. 116, no. 5, pp. 2742–2750, Nov. 2004.

[53] E. Z. Zhang, J. G. Laufer, R. B. Pedley, and P. C. Beard, "*In vivo* high-resolution 3D photoacoustic imaging of superficial vascular anatomy," *Phys. Med. Biol.*, vol. 54, no. 4, pp. 1035–1046, Feb. 2009.

Bradley E. Treeby, Benjamin T. Cox, Edward Z. Zhang, Sarah K. Patch, and **Paul C. Beard** photographs and biographies not available at time of publication.